Journal of Power Sources 208 (2012) 426–433

Contents lists available at SciVerse ScienceDirect

Journal of Power Sources

journal homepage: www.elsevier.com/locate/jpowsour

Tailoring structural and electrochemical properties of vertical aligned carbon nanotubes on metal foil using scalable wet-chemical catalyst deposition

S. Dörfler[a,b,*], I. Felhösi[c], I. Kék[c], T. Marek[c], H. Althues[a], S. Kaskel[a,b], L. Nyikos[c]

[a] Fraunhofer Institute for Material and Beam Technology (IWS) Dresden, Winterbergstraße 28, 01277 Dresden, Germany
[b] Institute for Inorganic Chemistry, Dresden, University of Technology, Bergstraße 66, 01069 Dresden, Germany
[c] Hungarian Academy of Sciences, Chemical Research Center, Institute of Nanochemistry and Catalysis, 1025 Budapest, Pusztaszeri ut 59-67, Hungary

ARTICLE INFO

Article history:
Received 17 November 2011
Received in revised form 14 February 2012
Accepted 17 February 2012
Available online 25 February 2012

Keywords:
Vertical aligned
Carbon nanotubes
Wet-chemical catalyst
Metal foil
Diameter control
Capacity

ABSTRACT

A scalable process for the synthesis of vertical aligned carbon nanotubes (VA-CNT) with precise control over structural properties is described. Direct growth on metal foils is achieved using a dip-coating step for the wet-chemical catalyst layer deposition and a subsequent chemical vapor deposition step for CNT growth. Two optimized Fe/Co and Fe/Mo 2-ethylhexanoate/2-propanol solutions are applied as precursors for the catalyst layer deposition and the influence of catalyst film thickness on resulting CNT film properties is investigated. The catalyst layer thickness can be controlled by the precursor salt concentration in the dip coating solution. By using a Fe and Co (2:3 ratio) catalyst, the CNT film homogeneity dramatically drops with lowered catalyst concentration due to a strong Ostwald ripening behavior of the catalyst layer. By using the FeMo (47:3 ratio) catalyst system, homogeneous VA-CNT films are obtained and the average CNT diameter can be adjusted in a range of 5–20 nm by the catalyst layer thickness. The electrochemical properties of the CNT electrodes are investigated in a symmetric supercapacitor test cell. The lowest CNT diameters of 5 nm results in a specific double layer capacitance up to 60 F g^{-1}, while the density of the films directly correlates with its pore resistance.

1. Introduction

The efficient synthesis of vertical aligned carbon nanotube (VA-CNT) films via chemical vapor deposition (CVD) growth – also named "super growth" was discovered 2004 by Hata et al. [1,2] and has been intensively studied since then. Most promising applications are field emission displays [3–5], lithium ion cells, optical polarizers [2,6], gas sensors [7], heat conductors and electrochemical double layer capacitors (EDLC) [2]. VA-CNT have a high intrinsic conductivity, an ordered pore structure and a direct binder-free contact between substrate and CNT.

For the scalable production of VA-CNT based electrodes atmospheric pressure deposition techniques and direct synthesis of VA-CNT on conductive substrates need to be developed. Furthermore, a good control over diameter, length and density is necessary. Especially in EDLC electrodes, the CNT diameter influences the specific surface area correlating directly with the gravimetric capacity.

For the CNT growth via CVD, catalyst nanoparticles can be deposited by low pressure physical vapor methods [8] or wet-chemical techniques [9]. The synthesis of particles has the advantage that particle diameter and with it the CNT diameter can be easily predicted. Low pressure techniques for particle growth suffer from high investments necessary for up-scaling. Wet-chemical particle syntheses on the other hand need additional time consuming productions steps and the resulting particle dispersions tend to agglomerate and are thus not stable.

The other approach to achieve a dense particle network is to deposit metal or oxidized metal films being thermally treated and reduced by hydrogen or hydrocarbons. Most frequently used are low pressure physical vapor techniques to deposit the conformal catalyst film coatings on the substrate [1,10–13]. CNT diameter can be adjusted by the catalyst layer thickness [14].

An alternative route is the wet-chemical catalyst deposition using metal nitrates, chlorides and acetates in polar organic solvents such as ethanol and methanol [15–18,6] deposited mostly for low-pressure CVD processes. Precursor solutions can be applied via dip-coating which is essential for the development of scalable processes. In a previous work, the direct homogenous growth on nickel foils by an atmospheric pressure (AP) CVD process and

* Corresponding author at: Fraunhofer Institute for Material and Beam Technology (IWS) Dresden, Winterbergstraße 28, 01277 Dresden, Germany.
Tel.: +49 351 83391 3182; fax: +49 351 83391 3300.
E-mail addresses: susanne.doerfler@iws.fraunhofer.de (S. Dörfler), ifelhosi@chemres.hu (I. Felhösi), kek.ildiko@chemres.hu (I. Kék), tamas.marek@chemres.hu (T. Marek), holger.althues@iws.fraunhofer.de (H. Althues), stefan.kaskel@chemie.tu-dresden.de (S. Kaskel), nyikos@chemres.hu (L. Nyikos).

0378-7753/$ – see front matter © 2012 Elsevier B.V. All rights reserved.
doi:10.1016/j.jpowsour.2012.02.067

wet-chemical catalyst coating based on alcoholic Fe, Co and Mo complex solutions has been demonstrated [19].

In this work, the CNT morphology, density and diameter can be controlled by the Fe, Co and Mo complex concentrations in an alcoholic dip-coating solution. For the AP-CVD process, ethene as carbon precursor was used. The resulting catalyst layers were investigated by AFM and the CNT films by SEM, TEM, Raman spectroscopy and electrochemical characterization methods such as impedance spectroscopy and galvanostatic charge–discharge measurements.

2. Materials and methods

The detailed synthesis of the Al_2O_3 and oxidized Co, Fe and Mo alloy layers and the subsequent CVD process for the VA-CNT growth has been described elsewhere [19].

2.1. Characterization methods

The as deposited, thermally treated and reduced catalyst or rather buffer layer properties are investigated by an atomic force microscope (AFM) NANOSCOPE (DIGITAL INSTRUMENTS) in tapping modus. For the analyses, tips made of n-doped silicon type RTESP (VEECO) are used. All images are shown in topography contrast. The oxidized catalyst layer thicknesses are also measured by AFM on silicon: the as deposited catalyst layer was scratched by a razorblade and the resulting edge was investigated with the AFM tip. Ten generated profile sections of each sample were measured. The evaluation of the catalyst layer thickness by ellipsometry was not possible due to the alloyed layer and the small thickness. The measurement of the catalyst thicknesses both by ellipsometry and AFM on nickel foil was not possible because of high surface roughness (25 nm).

The detailed characterization of the CNT films or rather scratched-off CNT by Raman spectroscopy, scanning electron microscopy (SEM) and transmission electron microscopy (TEM) is described elsewhere [19]. TEM resolution is limited so that no exact information about the number of CNT walls can be obtained.

Nitrogen adsorption is carried out with a surface area and pore size analyzer QUANTACHROME QUADRASORB SI. The specific surface area (SSA) is calculated by using the (BET) multipoint model and the values between 0.05 and 0.1 p/p_0. For one measurement, the CNT films of eight substrates (3.5 cm × 3.5 cm) were scratched-off.

2.2. Cell assembly

All samples for the electrochemical tests are assembled in a flat test cell consisting of a stainless steel (SS) current collector and a Teflon body. An ethylcellulose separator with 25 μm thickness (NIPPON KODOSHI CO.) is placed between two identical CNT-coated Ni foil electrodes (area of each electrode: 1 cm × 1 cm). The diameter of the SS current collector is 8 mm, designed to be lower than the surface area of CNT electrodes in order to minimize the effect of extra metal/electrolyte interface on electrochemical measurements. 1 g $TEABF_4$ (FLUKA, for electrochemical analysis = 99.0%) dissolved in 10 ml acetonitrile (ACROS ORGANICS, 99.9%, extra-dry, water content < 0.001%) is used as electrolyte. The electrolyte preparation and cell assembly are carried out in a glove-box under argon atmosphere. The total internal resistance of metallic cell components (without CNT electrodes, separator and electrolyte) and instrumentation is 48 mΩ and was taken into account in calculation of resistive elements.

2.3. Electrochemical measurements

During all the electrochemical measurements the test cell is placed in a glove-box under argon atmosphere, and the room temperature is kept at 25 °C.

The impedance spectra are obtained with a SOLARTRON 1286 electrochemical interface and a 1250 frequency response analyzer in the frequency range from 65 kHz to 100 mHz with 10 points per decade using 10 mV amplitude. The data analysis is performed using ZWIEV software by fitting impedance spectra to equivalent circuit models. The cell stability was evaluated with a SOLARTRON 1286 electrochemical interface by performing galvanostatic charge/discharge cycles with a constant current of 1 A g^{-1} between 0 V and 2 V up to 2000 cycles. The discharging capacitance was determined by integration of corresponding voltage–time curves.

The cell capacitance values obtained in the symmetric cell configuration were recalculated also to a single electrode capacitance. This latter is four times larger than the value of cell capacitance measured in a two-electrode cell configuration. The 1:4 ratio is due to the serial connection of two identical capacitor with twice the mass or twice the surface area resulting *cell* capacitance value per mass or per area is one fourth of the same number characteristic to the single electrode capacitance.

3. Results and discussion

As described in a previous publication, the applied process chain includes the wet-chemical catalyst (oxidized Fe, Co and Mo) and buffer (Al_2O_3) coating procedure and the subsequent CVD process at 730 °C by using ethene as carbon precursor [19].

Orientation and height of the films after 20 min growth rate differ for the different catalyst compositions generated by 0.22 mol l^{-1} catalyst concentration: the highest carbon nanotube forests (170 μm) are observed with 40 mol% Fe and 60 mol% Co catalyst composition. Interestingly, a slight addition of 6 mol% Mo to the pure Fe complex without Co leads to lower, but denser nanotube forests. For the samples with pure Fe layer and the optimized Fe:Co (2:3) composition, only multi-walled CNT could be observed. For the Fe:Mo (47:3) catalyst system, Raman spectra indicate the presence of single-walled or rather double-walled CNT. The specific surface area (SSA) of the scratched-off CNTs grown after 20 min by Fe:Co (2:3) catalyst composition is 248 m^2 g^{-1} (BET) and 265 m^2 g^{-1} (BET) by FeMo (47:3).

3.1. CNT films

One approach to decrease the MWNT diameter is to reduce the catalyst complex concentration in the dip-coating solution and therefore, to drop the catalyst layer thickness on nickel substrate [14,20]. In this work, the catalyst film thickness for both the Fe:Co (2:3) and the Fe:Mo (47:3) system is lowered by decreasing the catalyst precursor concentration in the dip-coating solution. Table 1 shows the applied catalyst complex concentrations, the

Table 1
Applied catalyst complex concentrations, the resulting oxidized catalyst layer thickness and CNT mass per area after CVD process.

Catalyst conc. [mol l^{-1}]	Catalyst layer thickness [nm]	Active mass per area [mg cm^{-2}]
0.220	23.8	1.28
0.165	18.4	0.93
0.110	12.0	0.68
0.055	4.4	0.72
0.022	2.8	0.36
0.015	2.3	0.10

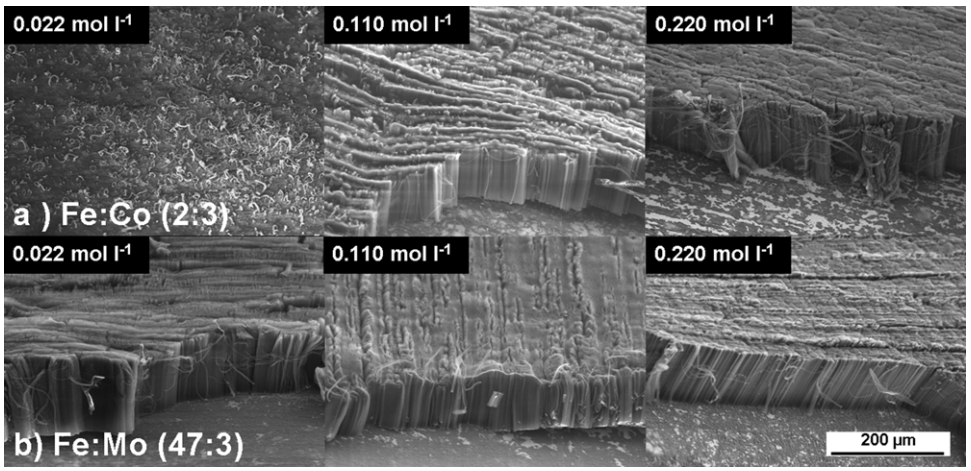

Fig. 1. SEM images of CNT films grown by three different catalyst concentrations on Ni foil (R_a = 25 nm) – comparison between (a) Fe:Co (2:3) and (b) Fe:Mo (47:3) catalyst system.

resulting oxidized catalyst layer thickness calculated by AFM and the CNT mass per area after CVD process. For 0.011 mol l^{-1}, the catalyst layer thickness could not be calculated since no difference between scratched-off and as-deposited layer could be observed. The thickness of this oxidized layer can be estimated as 1–2 nm.

For the production of a dense vertical aligned CNT forest by the described coating technique a Fe/Co 2-ethyhexanoate (2:3 ratio) concentration of at least 0.110 mol l^{-1} is necessary. Lower concentrations lead to a decreased film homogeneity and density and are not investigated further (Fig. 1a). For the reduced metal concentration of the Fe:Mo 47:3 catalyst system the CNT film homogeneity stays quite constant for 0.022 mol l^{-1} (Fig. 1b) even for 0.015 mol l^{-1} showing a completely different growth behavior compared to the optimized Fe:Co 2:3 catalyst system.

To have a closer understanding of the particle network evolution during the thermal treatment at process temperature and in situ reduction by hydrogen both optimized catalyst systems deposited on 30 nm Al_2O_3 and polished silicon were investigated by AFM: Fig. 2 shows images of the Fe:Co (2:3) and Fe:Mo (47:3) catalyst films as deposited (0.22 mol l^{-1} catalyst concentration), thermally and treated and reduced by hydrogen at 730 °C. It can be clearly seen that the as-deposited catalyst layer is smooth for both systems: the surface roughness for the Fe:Mo (47:3) and for the Fe:Co system is R_a = 0.2. By heating these similar smooth oxidized layers up to 730 °C the layer morphology changes differently for both catalyst systems, respectively. The oxidized Fe:Mo (47:3) catalyst layer becomes only slightly rougher (R_a = 0.5 nm) but the Fe:Co (2:3) oxide film morphology and roughness (R_a = 5.2 nm) totally changes. During the CNT growth the oxidized layers are reduced by hydrogen to generate a network of elemental metal particles being essential for the actual CNT growth. For the Fe:Mo (47:3) system a film roughness of R_a = 0.7 nm and for the Fe:Co (2:3) system R_a = 4.7 nm was calculated.

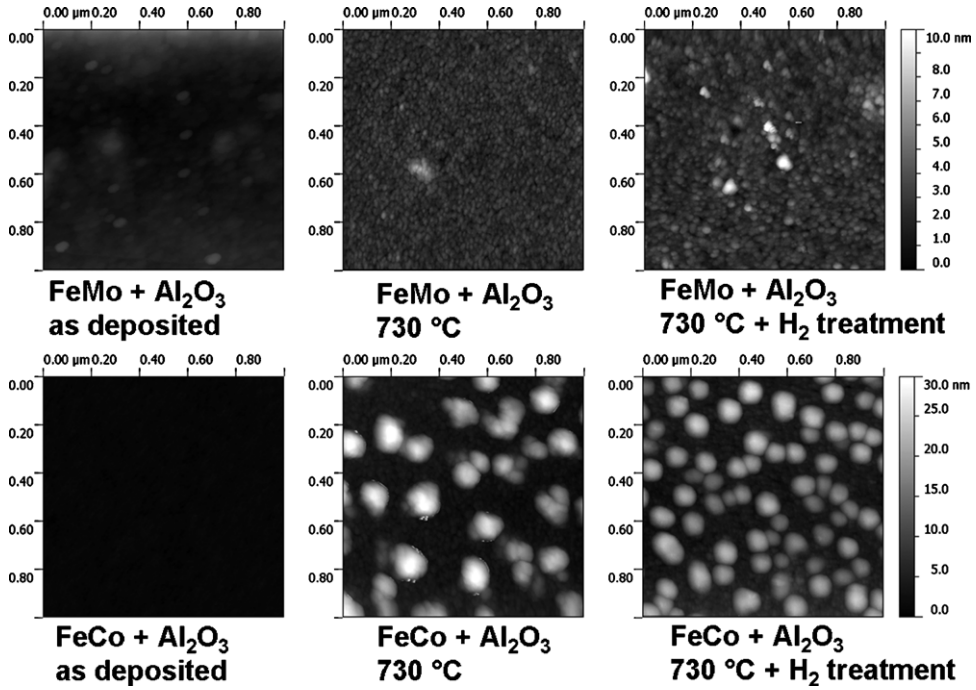

Fig. 2. AFM images of the Fe:Co (2:3) and Fe:Mo (47:3) catalyst films as deposited by 0.22 mol l^{-1} catalyst concentration, thermally treated and reduced by hydrogen at 730 °C.

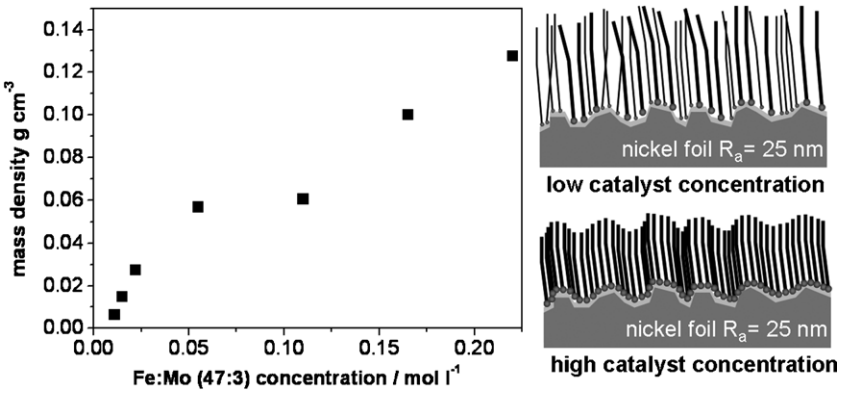

Fig. 3. CNT mass density with increasing catalyst concentration (l) and scheme how CNT growth is influenced by different catalyst concentrations (*r*).

Sugime et al. [21] observed that Mo addition suppresses the surface diffusion and hence, Ostwald ripening of Co catalyst atoms because Mo atoms have a larger radius than Co or rather Fe. Similar effects could be the reason for the density increase with 6 wt% Mo content in the Fe catalyst layer, since Fe and Co atom radii are similar. Both the simply thermally treated and the reduced catalyst layers give evidence for the different Ostwald ripening behaviors of the respective catalyst system being a precondition for the CNT diameter adjustment.

The CNT mass per area drops from 1.3 mg cm^{-2} to 0.09 mg cm^{-2} with decreasing catalyst layer thickness. In contrast, Zhao et al. [14] observed an increase of the CNT mass density with lower catalyst layer thicknesses on polished silicon as substrate. So the surface roughness of the metal foil seems to play an important role for the VA-CNT morphology.

Interestingly, the CNT height rises with lower catalyst concentration and with it lower catalyst layer thickness by investigation of 2.5 cm substrate length: for 23.8 nm (0.22 mol l^{-1}) the CNT film height is 101.1 ± 2.4 μm, for 12.0 nm (0.11 mol l^{-1}) 102.9 ± 27.5 μm and for 2.8 nm (0.022 mol l^{-1}) 135.9 ± 42.9 μm. The higher standard deviation indicates a more inhomogeneous growth with lower catalyst concentration.

The CNT film density (mass per volume) becomes remarkably lower with decreasing catalyst layer (Fig. 3). Reason for this could be the decreased quantity of CNT seeds that are formed on the substrate surface with lower catalyst concentration. If one CNT seed has less neighbored CNT seeds, the carbon precursor diffusion and the space being needed for the growth are much higher so that the CNT film becomes higher. Furthermore, SWNT intrinsically require less carbon per unit length, thus the growth rate is higher compared to MWNT, as well. [14]

Fig. 4a shows TEM images of CNT grown by different catalyst concentrations: the CNT diameter can be reduced dramatically by decreasing the catalyst complex concentration in the dip-coating solution and therefore the catalyst layer or rather particle diameter. By using 0.22 mol l^{-1} an oxidized catalyst thickness of ca. 24 nm could be synthesized. Half of this concentration (0.110 mol l^{-1}) generates a catalyst layer thickness of ca. 12 nm. For 0.022 mol l^{-1} and 0.015 mol l^{-1} the catalyst thicknesses could be decreased to 2.8 and 2.3 nm, respectively. Generally, due to the reductive hydrogen treatment the resulting particles are smaller. For lower concentrations (between 0.015 and 0.055 mol l^{-1}), the catalyst particles probably tend to agglomerate so that the resulting CNT diameter are higher than the oxidized layer thickness. For higher catalyst layers the resulting CNT diameters are smaller than the oxidized catalyst layers for two probable reasons: first, with increasing catalyst layer the catalyst particle tend less to agglomerate. Second, the catalyst layer of 24 nm thickness is roughened only superficially as can be seen in AFM section images of a FeMo catalyst layer profile on silicon.

Fig. 5 shows adsorption isotherms of scratched-off CNT grown by two different catalyst concentrations in the dip-coating solution: for 0.022 mol l^{-1} catalyst complex concentration the specific surface area of the resulting CNT film is increased from 265 to 506 m^2 g^{-1} compared to the SSA of CNT films prepared by ten fold higher concentration (0.220 mol l^{-1}) being in good agreement with the TEM images. Zhao et al. [14] obtained similar SSA values for triple walled nanotubes with diameters between 5 and 12 nm.

In Fig. 6 Raman spectra of CNT films prepared by three different catalyst concentrations are shown: With decreasing catalyst concentration in the dip-coating solution the ratio of the graphitic peak (G peak) and the peak representing disordered carbon (D-peak) increases from 0.4 to 0.7. Furthermore, the intensities of the so-called "Radial Breathing Modes" (RBM, 120–250 cm^{-1}) indicating DWNT and SWNT with a diameter between 1 and 2 nm [14,22] increases with lower catalyst concentration. The maximum of the most intensive peak at (230 cm^{-1}) corresponds to a CNT diameter of 1.08 nm. Furthermore, a smaller peak at 210 cm^{-1} from CNT grown by 0.022 mol l^{-1} catalyst concentration representing CNT with diameters of 1.18 nm arises. SWNT diameters can be calculated from the RBM intensity by following equation [22]:

$$d_{\mathrm{CNT}} = \frac{248\ \mathrm{cm^{-1}nm}}{\omega_{\mathrm{RBM}}} \quad (1)$$

Interestingly, for CNT grown by catalyst layers being deposited by a concentration of 0.015 mol l^{-1} no RBM can be observed although the corresponding TEM images show CNT with similar diameters (4.8 ± 1.1 nm) as CNT diameters generated by 0.022 mol l^{-1} catalyst concentration (4.5 ± 0.8 nm). Furthermore, the gravimetric capacity increases for CNT prepared by 0.015 mol^{-1} compared to CNT generated by 0.022 mol l^{-1} catalyst concentration being discussed in detail below (see Section 3.2.3).

Probable reasons for these observations are:

(1) Only CNT with diameters between 1 and 2 nm show RBM, for CNT being broader than 2 nm the RBM intensities are weak and only hardly observable but e.g. Zhao et al. [14] generated SWNT with diameters up to 8 nm. As indicated by TEM, for 0.11 mol l^{-1} catalyst concentration (12.0 nm catalyst layer), CNT diameter of 6.2 ± 4.7 nm and for 0.022 mol l^{-1} (2.8 nm catalyst layer thickness), CNT diameters of 4.5 ± 0.8 nm were observed. Possibly, only a small percentage of 1–2 nm broad CNT are generated by 0.11 and 0.022 mol l^{-1} catalyst concentration. The relatively low G/D peak area ratio (0.4–0.7) for all three samples indicate the presence of MWNT, as well. For 0.015 mol l^{-1} catalyst concentration, the catalyst particles may tend more to agglomerate

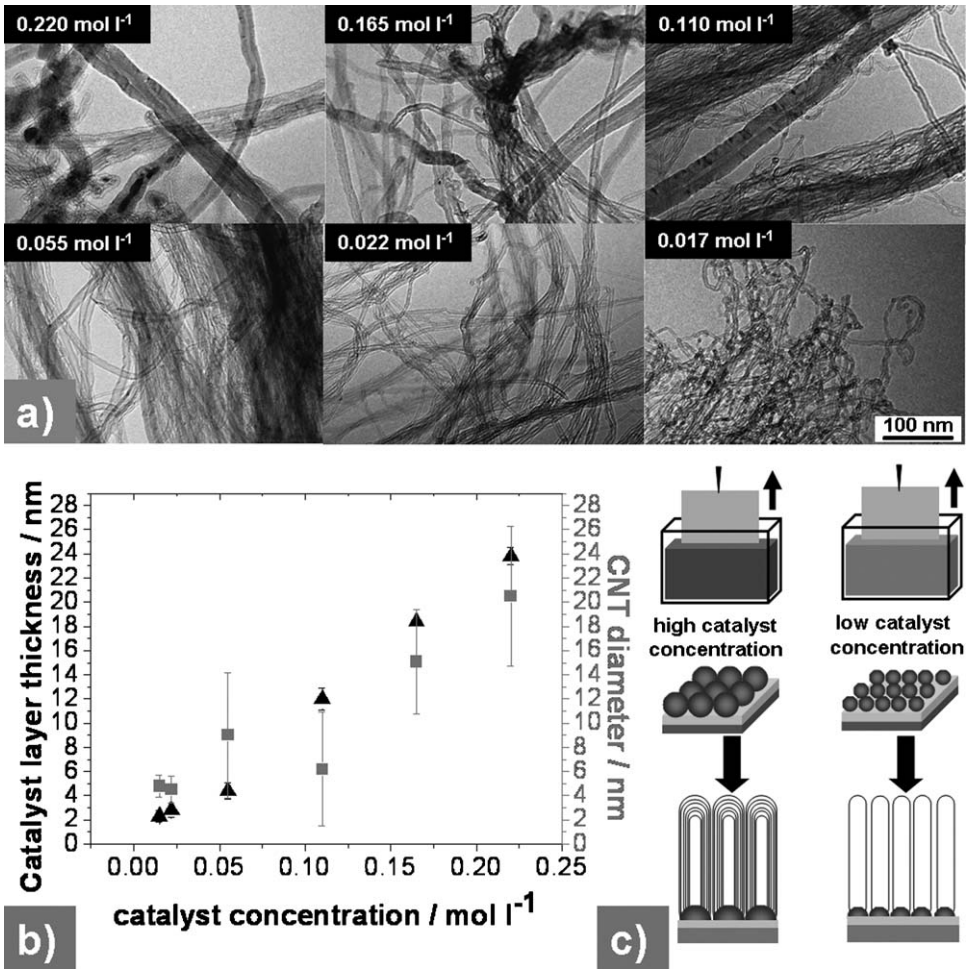

Fig. 4. (a) TEM images of scratched-off CNT grown by different catalyst complex concentration in the dip coating solution, (b) catalyst layer thickness and CNT diameter vs. catalyst concentration of the Fe:Mo (47:3) complex concentration in the dip-coating solution (c) and scheme of the CNT diameter control.

at the rough substrate surface so the CNT diameter cannot be decreased under 4.6 ± 0.9 nm and no nanotubes between 1 and 2 nm diameter are generated.

(2) Raman features depend on the resonance condition and with it on the excitation laser wavelength. Probably, with a slight decrease of the CNT diameters the resonance condition changes. In this work, Raman investigations were limited to two laser wavelengths (785 and 514 nm). For 514 nm laser excitation wavelength, a weak signal-to-noise ratio of the Raman spectra for all described samples could be observed indicating suboptimal resonance conditions. In a future work, the CNT synthesized using different catalyst layer thickness can be investigated with various excitation laser wavelengths close to 785 nm to realize a slightly different resonance condition.

3.2. Electrochemical characterization

3.2.1. Impedance spectra

Fig. 6a displays the impedance spectrum of a supercapacitor cell consisting of aligned CNT forest active layer grown on FeMo 47:3 catalyst layer generated by 0.165 mol l^{-1} catalyst complex concentration (18.4 nm oxidized catalyst layer, 0.93 mg cm^{-2} CNT). The impedance spectrum is also plotted after subtraction of inductance element. The impedance spectrum exhibits typical characteristics of porous electrodes without Faraday processes.

Spectra can be well fitted with the equivalent circuit model consisting of an inductance of instrumentation (wires) L, a serial resistance representing the internal resistance of the capacitor R_s, and the impedance of the porous layer Z_{por}. The internal serial resistance R_s is determined by the electrolyte resistance with some contribution of ohmic resistance of metal components and contact resistance between the active layer and substrate:

$$R_s = R_{\text{electrolyte}} + R_{\text{contacts}} + R_{\text{ohmic}} \quad (2)$$

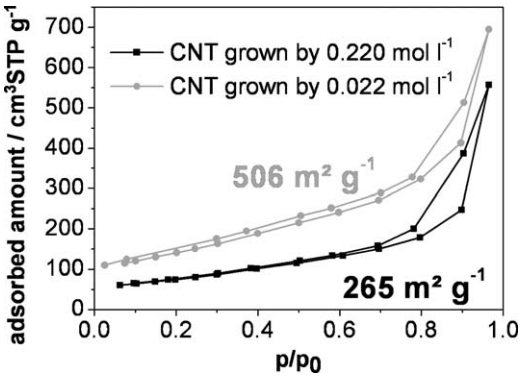

Fig. 5. Adsorption isotherms of scratched-off CNT grown by two different catalyst concentrations.

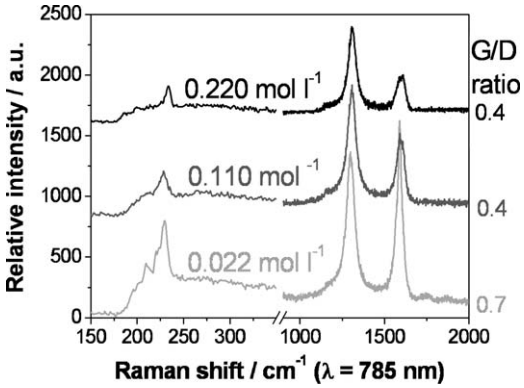

Fig. 6. Raman spectra of CNT grown by three different catalyst concentrations.

The impedance of porous layer Z_{por} can be described by a modified de Levie impedance element [23,24]:

$$Z_{por}(\omega) = \left(\frac{R_W}{j\omega C}\right)^n \coth(j\omega R_W C)^n, \quad (3)$$

where R_W represents the ion diffusion inside the pores, and C represents the low frequency capacitance, which is determined by the double layer capacitance of the total pore surface area. If $n = 0.5$, the impedance $Z(\omega)$ will be equal to the ideal de Levie impedance element, where the porous electrode is described by a RC-transition line model. Deviation of n from the ideal value of 0.5 is typical for real macroscopic porous electrodes.

The non-ideality may be interpreted as a result of several surface irregularities; such as distribution in macroscopic path lengths (non-uniform active layer thickness), distribution of pore size [25] or shape [26], or substrate/electrolyte boundary effect [27].

The low and high frequency limits of Eq. (3) are as follows:

At low frequency:

$$Z_{por}(0) = \left(\frac{1}{j\omega C}\right)^{2n} + \frac{R_W}{3} = \mathrm{CPE}_{dl} + R_{por}, \quad (4)$$

which is a serial combination of the pore resistance, and the double layer capacitance at the whole pore's surface, described by non-ideal constant phase element (CPE), representing the frequency dispersion. This frequency dispersion may be the result of combination of several types of surface heterogeneity [24].

At high frequency:

$$Z_{por}(\omega \to \infty) = \left(\frac{R_W}{j\omega C}\right)^n, \quad (5)$$

looks like the generalized Wartburg element, describing the ionic transport control inside the porous active layer, and is attributed to the low penetrability of pores.

As seen on the typical impedance spectrum shown in Fig. 7a, the impedance characteristics of CNT electrodes are very close to the ideal behavior, $n = 0.493$. Reasons for it are the aligned structure of CNT layer, the uniform length and the narrow distribution of pore diameter, the excellent electron conductivity of CNT and a very low contact resistance between the nickel substrate and CNT active layer.

The specific double layer capacitance of aligned CNT electrode sample (with catalyst layer formed in 0.165 mol l^{-1} concentration) calculated from impedance spectra at 2 V is 20 F g^{-1} (corresponding cell capacitance is 5 F g^{-1}, see also Fig. 8). This value is in agreement with the differential specific capacitance (19.44 F g^{-1}) calculated from the initial slope of galvanostatic discharge curve

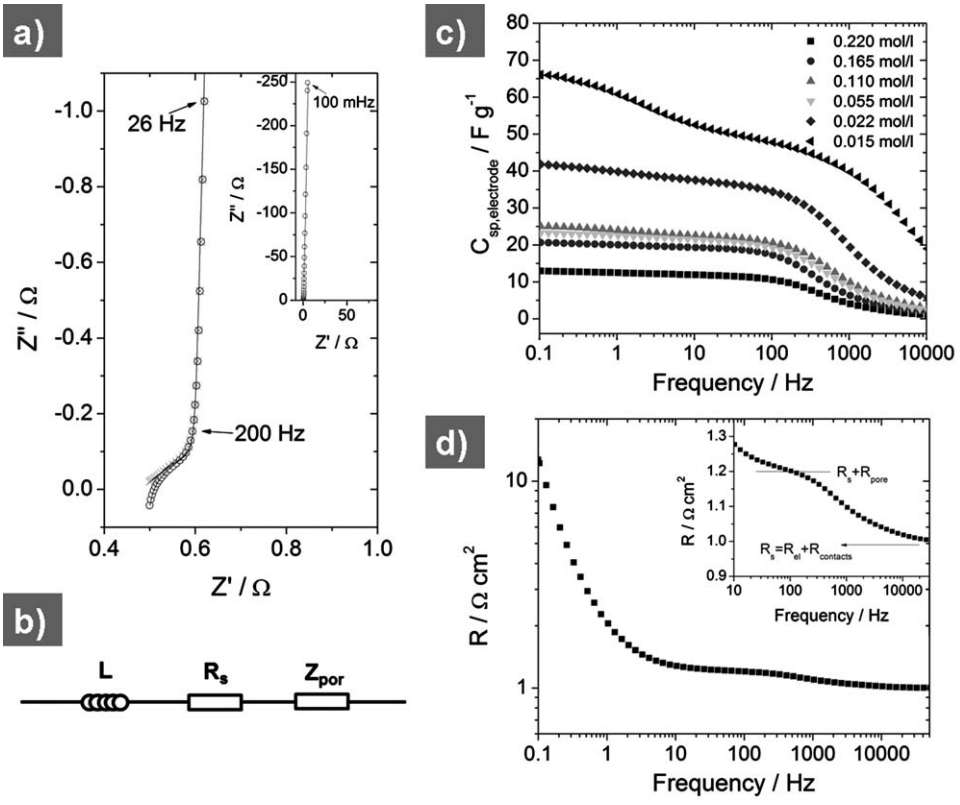

Fig. 7. (a) Complex plane impedance spectrum of a two-electrode symmetrical cell of CNT active layer (catalyst layer formed in 0.165 mol l^{-1} concentration of complex mixture). ○: measured impedance data, **x**: the same after subtraction of inductance from the spectra, solid lines: fitted curves based on the shown equivalent circuit (b); (c) apparent specific capacitance as a function of frequency. (d) normalized resistance as a function of frequency. (Data are obtained in a two-electrode symmetrical cell of 0.93 mg cm^{-2} CNT active layer (catalyst layer formed in 0.165 mol l^{-1} concentration of complex mixture) from impedance spectra measured at 2 V bias voltage.)

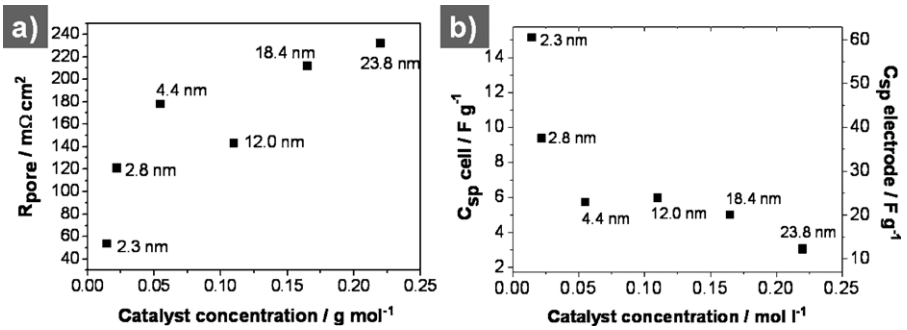

Fig. 8. Influence of catalyst concentration on (a) the pore resistance and (b) specific capacitance of the electrode. Data were obtained from impedance spectra at 2 V, the corresponding catalyst layer thicknesses are given in the graphs.

measured with 1 A g^{-1}. It is well below the achievable value of SWCNT of 80 F g^{-1} (20 F g^{-1} cell capacitance), which is presented in non-aqueous electrolytes [28,29]. The difference is due to the formation of MWCNT in large quantities, having lower accessible surface area, as presented in Raman spectra (Fig. 6), TEM images (Fig. 4) and the SSA (Fig. 5). The difference correlates with the lower BET surface area (265 m^2 g^{-1}) compared to the 1000 m^2 g^{-1} of Ref. [28].

The electrolyte resistance is very low, in between 0.25 and 0.45 Ω cm^2, which is 3–5 times higher than the theoretical value of electrolyte resistance (83 mΩ cm^2) calculating with 30 mS cm^{-1} conductivity and 25 μm distance between electrode plates. The difference may be due to the porosity and resistance of separator, and non-uniformity of the distance between the rigid nickel plates and contribution of the resistance of oxides present at the substrate.

The pore resistance, and therefore the barrier effect against ionic transport are very low, which is the consequence of the aligned structure of CNT layer. The pore resistance of 0.93 mg cm^{-2} (prepared by 0.165 mol l^{-1} catalyst concentration) CNT sample is 0.23 Ω cm^2, which is lower than the electrolyte resistance of 100 μm thick electrolyte film (0.3 Ω cm^2), indicating that the electrolyte penetrated into the whole depth of CNT forest layer and the whole outer CNT surface area is accessible to electrolyte. On the other hand, the smaller value indicates also that some horizontal tilting and densification of aligned CNT layer during preparation of cell may happen.

As a summary, the low electrolyte and pore resistance values of CNT based electrodes is beneficial for high-frequency or high power-density applications. The serial resistance

$$R_{esr} = R_{el} + R_{por} \tag{6}$$

being proportional to the CNT mass is 2.3 mΩ g. As an illustration, a hypothetical 100 F supercapacitor cell assembled from these CNT-based electrode materials would exhibit an estimated resistance originating from electrolyte and pores as low as 0.1 mΩ. This value is so low, that the total resistance of such a cell would be dominated by the ohmic resistance of its metallic components and the contacts.

3.2.2. Frequency dependence

Fig. 7c and d shows the frequency dependence of capacitance and resistance, where the apparent C and R values are calculated from the measured impedance data according to

$$C = \frac{-1}{j\omega Z''} \tag{7}$$

and $R = Z'$. The capacitance–frequency curve can be divided into two well-distinguishable ranges: (i) at low frequencies, $f < 200$ Hz, the capacitance is almost constant, the slight increase of capacitance with decreasing frequency is the result of the frequency dispersion due to macroscopic heterogeneity; (ii) at high frequencies, $f > 200$ Hz, the penetrability of pores in the active layer decreases with increasing frequency, therefore the capacitance drops. The real part component of impedance increases also with decreasing frequency: (i) at $f > 10$ kHz, the serial resistance R_s (dominantly the electrolyte resistance) is measured; (ii) in the middle range of 10–100 Hz the plateau relates to the sum of serial (electrolyte) resistance and the pore resistance, $R_s + R_{por}$, where the ions are able to access the whole electrode surface deep inside the pores, with the result of a longer pathway for the ions in the electrolyte [30]. (iii) At $f < 10$ Hz, a further increase of resistance occurs, which is a consequence of the real part component of the non-ideal CPE behavior of supercapacitor.

3.2.3. Influence of the catalyst layer thickness on the electrochemical characteristics

As presented in the previous part (Section 3.1), the thickness of catalyst layer has remarkable influence on the CNT density and the thickness of the walls of the formed CNT. Table 2 summarizes the impedance results of CNT electrodes generated by different catalyst layer thicknesses. It is known that double layer capacitance of carbonous materials in organic electrolytes depends on the applied voltage [29,30]. As supercapacitors are operated dominantly at a high voltage range, only differential double layer capacitance obtained at 2 V is given in this chapter.

As seen in Table 2, the increase of catalyst concentration and CNT density results in an increase of normalized double layer capacitance (specific to the surface area), and reaches a plateau

Table 2
Summary of the impedance data obtained with two-electrode cell of CNT electrodes with different active mass per surface area grown by different catalyst concentration.

Catalyst conc. [mol l^{-1}]	Catalyst layer thickness [nm]	CNT density [mg cm^{-2}]	C_{dl}[a] (2 V) [mF cm^{-2}]	C_{sp}[a] (2 V) [F g^{-1}]	R_{por} (2 V) [mΩ cm^2]
0.220	23.8	1.28	15.8	12.34	232
0.165	18.4	0.93	18.6	20.04	212
0.110	12.0	0.68	16.3	23.91	143
0.055	4.4	0.72	16.4	22.89	178
0.022	2.8	0.36	13.5	37.43	121
0.015	2.3	0.10	5.96	60.53	53.6

[a] Calculated to single electrode capacitance value.

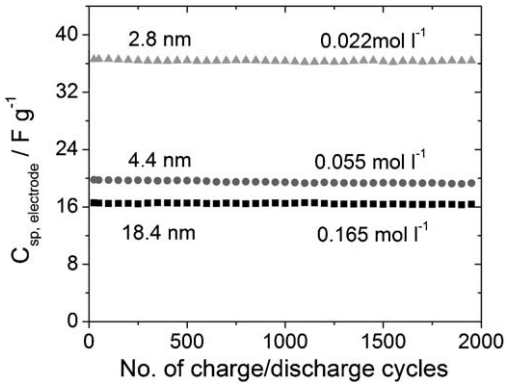

Fig. 9. Galvanostatic charge/discharge cycle stability measured at constant current of 1 A g^{-1} for VA-CNT electrodes prepared by different catalyst thicknesses. Specific discharge capacitance is given to single electrode value; the corresponding catalyst layer thickness is given in the graphs.

around 0.05 mol l^{-1} catalyst concentration; above this concentration only slight further increase in the double layer capacitance was observed. It suggests that above this concentration even if the mass of CNT layer is increasing, the BET surface area is nearly constant, due to the formation of MWCNT in higher ratio. The maximal surface area related capacitance was obtained with 0.165 mol l^{-1} catalyst concentration.

On the other hand the decrease of the catalyst concentration results in an increase of specific capacitance (Fig. 8b), which suggests that at low catalyst layer thicknesses (smaller particle size) the formation of thinner CNT is preferred. At very low catalyst concentration (0.015 mol l^{-1}) the resulting CNT film has 15 F g^{-1} cell capacitance (corresponding to 60 F g^{-1} single electrode specific capacitance), which is only little lower than the theoretical value of SWCNT (20 F g^{-1} [28,31]) in organic electrolytes. The pore resistance correlates also with the CNT catalyst layer thickness as visible in Fig. 8a. The increase of the catalyst layer thickness results in a denser CNT film. This evidently increases the porosity of the active layer, which consequently acts as a stronger barrier to ionic transport process.

3.2.4. Galvanostatic charge/discharge cycle stability of CNT electrodes

Fig. 9 illustrates the cycle stability properties of selected CNT cells. During the first 2000 cycles cell performance can be considered to be stable, less than 2% decrease of discharge capacitance were measured, which suggests long-cycle stability of CNT samples.

4. Conclusion

In conclusion, using an efficient dip coating process, a metal substrate and by using an optimized FeMo (47:3) catalyst system, the CNT diameter, specific surface area and gravimetric capacity could be controlled. The precursors for the wet-chemical catalyst layer deposition are affordable and available and the dip-coating process as well as the APCVD process has the potential for up scaling in a continuous process.

The specific capacitance observed on these samples approaches that of the theoretical maximum achievable for SWCNTs. With 0.0165 mol l^{-1} as catalyst concentration (corresponds to 2.3 nm oxidized catalyst layer) CNT with the highest specific capacitance (60 F g^{-1} for the single electrode) and very low pore resistance were generated (53.6–232 mΩ cm^2). The approach described demonstrates the feasibility of scalable production techniques being an important step towards CNT based binder-free nanoporous electrodes for energy storage applications.

In summary, electrochemical testing revealed the huge potential of the CNT-films for energy storage applications. Very low series resistance was measured indicating the applicability of CNT supercaps in areas where high power density or high frequency is crucial. However, the capacitance and therefore the energy density of the materials in the current state are different from our expectations. Only at high charging rates and in high-power applications CNT-electrodes are clearly advantageous over existing supercapacitor technologies.

Acknowledgements

This work has been supported by the European Commission under FP7 collaborative research project N2P contract number CP-IP 214134-2 and by the Free State of Saxony under ECEMP project (ENERCOAT subproject). We gratefully thank P. Németh (CRC Budapest) for the TEM investigations.

References

[1] K. Hata, D.N. Futaba, K. Mizuno, T. Namai, M. Yumura, S. Iijima, Science 306 (2004) 1362.
[2] K. Hata, S. Iijima, M. Yumura, D. Futaba, US Patent 2008/0318049 A1.
[3] T. Yamada, T. Namai, K. Hata, D.N. Futaba, K. Mizuno, J. Fan, M. Yudasaka, M. Yumura, S. Iijima, Nat. Nanotechnol. 1 (2006) 131.
[4] T. Hiraoka, T. Yamada, D.N. Futaba, H. Kurachi, S. Uemura, M. Yumura, S. Iijima, J. Am. Chem. Soc. 128 (2006) 13338.
[5] Y.M. Wong, W.P. Kang, J.L. Davidson, B.K. Choi, W. Hofmeister, J.H. Huang, Diamond Relat. Mater. 14 (2005) 2078.
[6] Y. Murakami, S. Chiashi, Y. Miyauchi, M. Hu, M. Ogura, T. Okubo, S. Maryama, Chem. Phys. Lett. 385 (2004) 298.
[7] W.S. Cho, S.-I. Moon, K.-K. Paek, Y.-H. Lee, Sens. Actuators B 119 (2006) 180.
[8] F. Schäffel, S. Schünemann, M.H. Rümmli, C. Täschner, D. Pohl, C. Kramberger, T. Gemming, A. Leonhardt, T. Pichler, B. Rellinghaus, B. Büchner, L. Schultz, Phys. Status Solidi B 245 (2008) 10, S.1919.
[9] H. Nishino, S. Yasuda, T. Namai, D.N. Futaba, T. Yamada, M. Yumura, S. Iijima, K. Hata, J. Phys. Chem. C 111 (2007) 17961.
[10] A.J. Hart, A.H. Slocum, J. Phys. Chem. B 110 (2006) 8250.
[11] S. Chakrabarti, H. Kume, L. Pan, T. Nagasaka, Y. Nakayama, J. Phys. Chem. C 111 (2007) 1929.
[12] S. Noda, K. Hasegawa, H. Sugime, K. Kakehi, Z. Zhang, S. Maruyama, Y. Yamaguchi, Jpn. J. Appl. Phys. 46 (No. 17) (2007) L399.
[13] Y. Yun, V. Shanov, Y. Tu, S. Subramaniam, M. Schulz, J. Phys. Chem. B 110 (2006) 23920.
[14] B. Zhao, D.N. Futaba, S. Yasuda, M. Akoshima, T. Yamada, K. Hata, ACS Nano 3 (1) (2009) 108.
[15] M. Someya, T. Fuji, US Patent 2003/0211029A1.
[16] M. Hu, Y. Murakami, M. Ogura, S. Maruyama, T. Okubo, J. Catal. 225 (2004) 230.
[17] N. Yoshikawa, T. Asari, N. Kishi, S. Hayashi, T. Sugai, H. Shinohara, Nanotechnology 19 (2008) 245607.
[18] L. Zhang, Y. Tan, D.E. Resasco, Chem. Phys. Lett. 422 (2006) 198.
[19] S. Dörfler, A. Meier, S. Thieme, P. Németh, H. Althues, S. Kaskel, Chem. Phys. Lett. 511 (2011) 288.
[20] I.K. Song, Y.S. Cho, G.S. Choi, J.B. Park, D.J. Kim, Diamond Relat. Mater. 13 (2004) 1210.
[21] H. Sugime, S. Noda, S. Maruyama, Y. Yamaguchi, Carbon 47 (2009) 234.
[22] M.S. Dresselhaus, G. Dresselhaus, R. Saito, A. Jorio, Phys. Rep. 409 (2005) 47.
[23] R. De Levie, in: P. Delaray, C.T. Tobias (Eds.), Advances in Electrochemistry and Electrochemical Engineering, 6, Interscience, NY, 1967, p. 329.
[24] R. Kötz, M. Carlen, Electrochim. Acta 45 (2000) 2483–2498.
[25] H.K. Song, Y.H. Jung, K.H. Lee, L.H. Dao, Electrochim. Acta 44 (1999) 3513–3519.
[26] H. Keiser, K.D. Beccu, M.A. Gutjahr, Electrochim. Acta 21 (1976) 539–543.
[27] J. Bisquert, Phys. Chem. Chem. Phys. 2 (2000) 4185–4192.
[28] D.N. Futaba, K. Hata, T. Yamada, T. Hiraoka, Y. Hayamizu, Y. Kakudate, H. Hatori, M. Yumura, S. Iijima, Nat. Mater. 5 (2006) 987–994.
[29] P.W. Ruch, L.J. Hardwick, M. Hahn, A. Foelske, R. Kötz, A. Wokaun, Carbon 47 (2009) 38–52.
[30] F. Rafik, H. Gualous, R. Gallay, A. Crausaz, A. Berthon, J. Power Sources 165 (2007) 928–934.
[31] L. Yang, B.H. Fishbine, A. Migliori, L.R. Pratt, J. Am. Chem. Soc. 131 (2009) 12373–12376.